collisions on the lower-level atomic polarization by supposing that this polarization is affected by depolarizing rates which increase exponentially with depth in the solar atmosphere. Assuming the same exponential behaviour for the absorption coefficient in the sodium lines, equation (2) becomes

$$Q/I = w\left(x_\nu + \frac{[x'_\nu]_0 - [x''_\nu]_0}{1+\alpha/k_\nu}\right) \qquad (3)$$

where $[x'_\nu]_0$ and $[x''_\nu]_0$ are the quantities x'_ν and x''_ν evaluated at the top of the solar atmosphere (where the alignment parameters are $[\beta_1]_0$ and $[\beta_2]_0$, respectively), k_ν is the line absorption coefficient, and α is a constant related to the scale height of the solar atmosphere.

The polarization profile resulting from equation (3) is shown in Fig. 1b (dashed line). In spite of the approximations, the agreement between the theoretical result and the observed polarization profile is striking. Not only does the model explain the appearance of sharp polarization peaks in the cores of the D_1 and D_2 lines but it also reproduces quite well the three-lobed profile of D_2: I conclude that ground-level atomic polarization exists in the top layers of the solar atmosphere.

The existence of ground-level atomic polarization has important implications for solar physics. Because such polarization is much more sensitive to depolarizing mechanisms than upper-level atomic polarization, it can be used as a sensitive tool for diagnosing extremely weak magnetic fields through the ground-level Hanle effect. In my approximate model, ground-level atomic polarization turns out to be of the same order of magnitude (and indeed slightly larger) as the upper-level atomic polarization, implying the absence of depolarizing effects (both due to collisions and to magnetic fields) in the layers of the atmosphere where the cores of the D_1 and D_2 lines are formed. Although magnetic fields slightly inclined with respect to the vertical are not ruled out (a magnetic field of the order of 1 G and inclined by as much as 10–20° with respect to the vertical is compatible with the observations), the constraints on turbulent and/or canopy-like fields are much more severe. A turbulent field of the order of 1 G, for instance, would practically destroy ground-level atomic polarization, so that a polarization profile similar to the dashed line in Fig. 1a would result. The same is also true for horizontal fields of the same order with randomly distributed azimuth.

The results reported here seem to rule out the existence in the lower solar chromosphere of magnetic fields stronger than about 0.01 G either in the form of volume-filling, turbulent fields or in the form of canopy-like, horizontal fields. This contradicts previous evidence, supported both by observations[3–8] and theory[16], for existence of turbulent magnetic fields as strong as 10–20 G in the solar atmosphere outside active regions; however, this evidence mainly refers to the upper photosphere and to the layers where the 4,607-Å Sr I line is formed, ~200 km below the layers considered here. The results also contradict the evidence for the existence of canopy-like fields in the solar chromosphere[9,10].

A paradox therefore seems to exist; on the one hand the success of my theory in explaining the polarization profile of the sodium doublet demonstrates the presence of ground-level atomic polarization. On the other hand, this polarization cannot survive in the presence of turbulent or canopy-like fields stronger than about 0.01 G, which contradicts previous evidence. Resolution of this apparent paradox could be obtained if all the turbulent fields of the upper photosphere reconnect very efficiently at a level roughly corresponding to the temperature minimum, so that in the lower chromosphere only vertical (or quasi-vertical) fields survive. But this condition seems to be very *ad hoc* and implies the presence of some physical mechanism not yet understood. □

Received 12 September; accepted 29 December 1997.

1. Stenflo, J. O. & Keller, C. U. New window for spectroscopy. *Nature* **382,** 588 (1996).
2. Stenflo, J. O. & Keller, C. U. The second solar spectrum. A new window for diagnostics of the Sun. *Astron. Astrophys.* **321,** 927–934 (1997).
3. Stenflo, J. O. Small-scale magnetic structures on the Sun. *Astron. Astrophys. Rev.* **1,** 3–48 (1989).
4. Stenflo, J. O. *Solar Magnetic Fields* (Kluwer, Dordrecht, 1994).
5. Faurobert-Scholl, M. Investigation of microturbulent magnetic fields in the solar photosphere by their Hanle effect in the SrI 4607 Å line. *Astron. Astrophys.* **268,** 765–774 (1993).
6. Faurobert-Scholl, M., Feautrier, N., Machefert, F., Petrovay, K. & Spielfiedel, A. Turbulent magnetic fields in the solar photosphere: diagnostics and interpretation. *Astron. Astrophys.* **298,** 289–302 (1995).
7. Stenflo, J. O., Keller, C. U. & Gandorfer, A. Differential Hanle effect and the spatial variation of turbulent magnetic fields on the Sun. *Astron. Astrophys.* **329,** 319–328 (1998).
8. Bianda, M., Solanki, S. K. & Stenflo, J. O. Hanle depolarisation in the solar chromosphere: The CaI 4227 Å line. *Astron. Astrophys.* (in the press).
9. Jones, H. P. & Giovanelli, R. G. Magnetic canopies in unipolar regions. *Solar Phys.* **87,** 37–42 (1983).
10. Solanki, S. K. & Steiner, O. How magnetic is the solar atmosphere? *Astron. Astrophys.* **234,** 519–529 (1990).
11. Happer, W. Optical pumping. *Rev. Mod. Phys.* **44,** 169–249 (1972).
12. Landi Degl'Innocenti, E. The density matrix approach to polarized radiative transfer. *Solar Phys.* **164,** 21–28 (1996).
13. Trujillo Bueno, J. & Landi Degl'Innocenti, E. Linear polarization due to lower-level depopulation pumping in stellar atmospheres. *Astrophys. J.* **482,** L183–L186 (1997).
14. Landi Degl'Innocenti, E., Landi Degl'Innocenti, M. & Landolfi, M. in *Forum Themis* (eds Mein, N. & Sahal Bréchot, S.) 59–77 (Observatoire de Paris, 1996).
15. Shurcliff, W. A. *Polarized Light* (Harvard Univ. Press, Cambridge, Mass., 1966).
16. Petrovay, K. & Szakály, G. The origin of intranetwork fields: a small-scale solar dynamo. *Astron. Astrophys.* **274,** 543–554 (1993).
17. Landolfi, M. & Landi Degl'Innocenti, E. Polarization of the sodium D lines in prominences. *Solar Phys.* **98,** 53–66 (1985).

Acknowledgements. I thank J. O. Stenflo for helping in the presentation of the Letter and for providing the original data shown in Fig. 1.

Correspondence and requests for materials should be addressed to E.L.D. (e-mail: landie@arcetri.astro.it).

Tunnelling and zero-point motion in high-pressure ice

Magali Benoit*, Dominik Marx† & Michele Parrinello†

* *Laboratoire des Verres, Université Montpellier II, 34095 Montpellier, France*
† *Max-Planck-Institut für Festkörperforschung, Heisenbergstrasse 1, 70569 Stuttgart, Germany*

The microscopic structure of ice poses a long-standing challenge to theory[1–3]. Because of their low mass, the protons in the hydrogen bonds that define the structures of crystalline ice are susceptible to quantum-mechanical effects such as tunnelling[1,4–8]. High pressure provides a means of controlling the length of the hydrogen bonds in order to investigate such effects. In particular, Holzapfel predicted 26 years ago that, under pressure, hydrogen bonds might be transformed from the highly asymmetric O–H···O configuration to a symmetric state in which the proton lies midway between the two oxygens[9], leading to a non-molecular symmetric phase of ice, now denoted as ice 'X'. The existence of this phase has been inferred from spectroscopy[10–14], but has still not been observed directly. Here we investigate the role of quantum effects in proton ordering and hydrogen-bond symmetrization within ice at high pressure by using a simulation technique that treats both electrons and nuclei quantum-mechanically[15–17]. We find that the proton-ordered structure at low pressure, with asymmetric hydrogen bonds (ice VIII), transforms on increasing pressure to a proton-disordered asymmetric phase (ice VII) owing to translational proton tunnelling. On further compression, the zero-point fluctuations lead to strongly delocalized protons and hydrogen-bond symmetrization, even though the underlying character of the proton-transfer potential remains a double well. Only at still higher pressures does the double-well potential become transformed into a single well, whereupon the protons again become increasingly localized.

The rich phase diagram of ice reduces to two known molecular ice phases above about 2 GPa, ice VIII and VII (ref. 18). Ice VII is best understood as being composed of two interpenetrating but not interconnected tetrahedral hydrogen-bonded networks of water molecules of normal cubic ice, I_c, with a body-centred-cubic

Nature © Macmillan Publishers Ltd 1998

(b.c.c.) oxygen structure. The orientation of the water molecules is random, apart from short-range order imposed by obeying the local 'ice rules'[18]. Contrary to this paraelectric phase VII, the water molecules and the associated dipole moments on the two sublattices do possess long-range order and point in opposite directions in the antiferroelectric phase VIII; the dipolar ordering is accompanied by a slight tetragonal distortion of the cubic unit cell along the staggered polarization axis[19]. The antiferroelectric disordering transition is characterized by a significant and constant H/D isotope effect of about 10 GPa below ~100 K, where the transition pressure (62 GPa for H_2O and 72 GPa for D_2O) is independent of temperature[10,11].

In the conjectured symmetric ice X (ref. 9), the oxygen lattice remains b.c.c., while the protons reside midway between their two nearest oxygen neighbours, instead of forming one covalent O–H and one H···O bond as in all low-pressure molecular phases such as ice VIII and VII. Despite numerous claims in the literature to have detected ice X, so far only infrared experiments have provided evidence for a transition towards a symmetrized structure at 60–70 GPa (~10 GPa higher for D_2O) in the range from room temperature down to at least 80 K (refs 12–14). However, the spectra are found to be congested as a result of various resonance phenomena[14,20,21], rendering their interpretation difficult. The symmetrization issue has been given a new twist by the idea[22–24] that two such forms might exist, namely 'proton-disordered symmetric ice' and 'proton-ordered symmetric ice'; see also refs 12, 14.

Here we approach these open questions based on our *ab initio* path integral technique[15–17], which satisfies all essential requirements posed by this complex system. Briefly, we treat all nuclei fully quantum-mechanically using path integrals[25] without reducing the dimensionality[4] or invoking other approximations[4] such as the quasiclassical or quasiharmonic ones[7,8], except that of neglecting the exchange of identical particles. The forces on the nuclei are derived for every individual configuration within the Born–Oppenheimer approximation from first-principles electronic structure calculations in the framework of Hohenberg–Kohn–Sham density functional theory[26], allowing chemical bonds to be broken and made. In view of the computational costs involved, no correction for the finiteness of the system, such as finite-size scaling and Trotter extrapolation techniques[25], could be applied. The conversion of the simulation cell volume to pressure is based on the standard experimental equation of state[27]. Thus, the pressure scale including the reported approximate transition pressures cannot be considered as precise numbers.

The degree of the antiferroelectric order is measured as the difference between the two sublattice polarizations of ice VIII. Our order parameter D (see Fig. 1 legend for definition) is about 1.2 qÅ in ideal ice VIII, whereas it drops to zero in an infinitely large 'perfect' paraelectric ordered structure. The fully quantum-mechanical simulations at 100 K (Fig. 1, filled circles) clearly start out in ice VIII at our lowest pressure. On compression, the order parameter stays close to the ideal value 1.2 qÅ but drops significantly at ~47 GPa down to a plateau value of ~0.4 qÅ up to the highest pressure. The simulation with classical nuclei at 100 K (Fig. 1, open circles) follows a similar pattern, but the antiferroelectric disordering now takes place at nearly twice the pressure (~76 GPa). A classical reference calculation at 300 K in the disordered phase VII (Fig. 1, squares) shows that the residual order of ~0.4 qÅ is due to local short-range correlations imposed by the ice rules[18] in conjunction with the limited system size and the periodic boundary conditions.

The symmetrization of the hydrogen bonds is best followed in

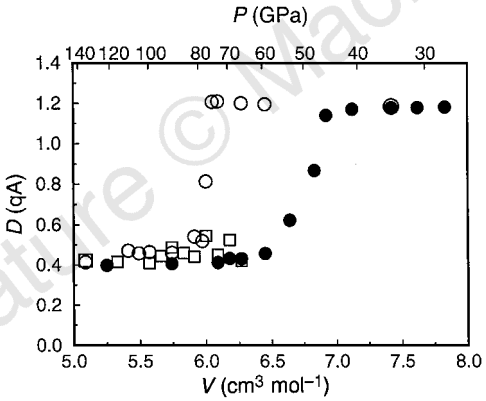

Figure 1 Antiferroelectric staggered order parameter D as a function of the molar volume V. We define D as the difference between the two sublattice polarizations 'up' and 'down', $D = \langle (1/N) \,|\, \Sigma^{N/2}_{j \in \mathrm{up}} \mathbf{d}_j - \Sigma^{N/2}_{j \in \mathrm{down}} \mathbf{d}_j | \rangle$, where $\mathbf{d}_j$ is the purely geometric dipole moment vector of the jth water molecule obtained with the formal charges $-2q$ and $+1q$ on oxygen and hydrogen atoms, respectively. Filled circles: quantum nuclei at 100 K; open circles: classical nuclei at 100 K; open squares: classical nuclei at 300 K. The conversion of the simulation cell volume to pressure is based on the experimental H_2O equation of state at 300 K (ref. 27); note that the H/D isotope effect on this quantity is as small as the experimental uncertainty[24]. All calculations were made with 16 H_2O molecules in a periodic cubic cell relying on a gradient-corrected[31] local density approximation[32], Troullier–Martins pseudopotentials[33] and a Γ-point plane wave expansion of the valence orbitals up to 70 Rydberg. The path integrals[25] for the quantum simulations[15,16] were discretized in imaginary time using 16 replica. The staging propagator together with one chain of three Nosé–Hoover thermostats per degree of freedom was used to improve sampling efficiency, ensure ergodicity and generate the canonical ensemble[17]. After careful equilibration, statistical averages were sampled from about 10,000 and 30,000 configurations in the quantum and classical cases, respectively.

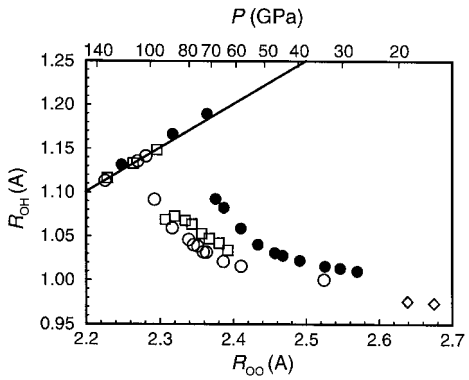

Figure 2 Evolution of the average oxygen–hydrogen bond length R_{OH} as a function of the average oxygen–oxygen distance R_{OO}. Filled circles: quantum nuclei at 100 K; open circles: classical nuclei at 100 K; open squares: classical nuclei at 300 K; open diamonds: experimental (R_{OO}, R_{OH}) data at about 240 K (ref. 28); solid line: 'symmetrization line' $R_{OH} = R_{OO}/2$, indicating ice X. For pressure conversion, see Fig. 1; note that as we plot the experimental data directly as (R_{OO}, R_{OH}) pairs, their corresponding pressure in this figure results from our pressure conversion according to ref. 27.

Nature © Macmillan Publishers Ltd 1998

Nature © Macmillan Publishers Ltd 1998

Fig. 2 by monitoring the evolution of the quantum-statistical average of the shortest oxygen–hydrogen bond length R_{OH} as a function of the neatest-neighbour oxygen–oxygen distance R_{OO} (which in turn is a function of pressure), the signature of symmetric ice simply being $R_{OH} = R_{OO}/2$ (solid line). We find this relation to be approximately linear in the low pressure regime, which has also been found by neutron scattering up to 10 GPa (ref. 19) and 20 GPa (ref. 28, and S. Klotz, personal communication). On compression, however, we find that the lengthening of the R_{OH} bond becomes much more pronounced as a function of decreasing R_{OO}. The quantum system (Fig. 2, filled circles) finally undergoes a symmetrization transition at ~72 GPa, whereas in the corresponding classical system (Fig. 2, open circles) a much higher pressure of ~102 GPa is needed to break the molecules apart. So far we have found that at ~100 K, phase VIII does not transform immediately into symmetric ice: there is clear evidence that proton-disordered molecular ice VII exists between proton-ordered ice VIII at lower pressures and symmetric non-molecular ice X at higher pressures.

At this stage we can go beyond experiment by unravelling the physical mechanisms that lead to the observed isotope effects by comparing the quantum simulations to the classical ones under the same conditions; furthermore, such a comparison yields theoretical upper bounds for the H/D isotope effects on the phase transitions, as quantified in Figs 1 and 2. To this end, we have analysed (Fig. 3) the average proton distribution $P(\delta, R_{O_aO_b})$ as a function of the proton position relative to the bond midpoint $\delta = R_{O_aH} - R_{O_bH}$ and the corresponding oxygen–oxygen separation $R_{O_aO_b}$. The quantum simulations shown in Fig. 3a and b correspond to ice VIII and VII, respectively, whereas those in Fig. 3c, d correspond to ice X. In ice VIII (Fig. 3a) the quantum fluctuations only induce a zero-point motional broadening of the distribution relative to the classical case (Fig. 3e), without affecting its shape. The quantum effects in ice VII (Fig. 3b) are dramatic, where it is proton tunnelling along the hydrogen bonds, absent in the classical case Fig. 3f, that leads to proton disorder and thus to a bimodal distribution. Finally, in ice X (Fig. 3c) we find a broad and flat but unimodal distribution centred at $\delta = 0$, which sharpens upon further compression (Fig. 3d). In contrast, the classical calculation (Fig. 3g) is characterized by a bimodal distribution, reflecting an underlying double-well proton-transfer effective potential. Taking into account that the thermal fluctuations correspond to the same temperature in Fig. 3c and g, it is a zero-point motion effect which shifts the lowest vibrational level of the proton wavefunction above the double-well barrier. This form of ice (Fig. 3c) could be dubbed 'proton-disordered symmetric ice' with delocalized protons because the proton distribution function is very broad, covers both potential wells, but peaks at the bond midpoint, $\delta = 0$. Only at still higher compression of $\geqslant 102$ GPa (from Fig. 2) do we observe a single well (Fig. 3h) with the potential minimum right at the centred position $\delta = 0$, which in turn could be called 'proton-ordered symmetric ice' (Fig. 3d) with localized protons at the bond midpoints; see refs 12, 14, 22–24 for earlier conjectures along these lines. Thus, we trace back the measured H/D isotope effects on the ice VIII → VII and symmetrization transitions to proton tunnelling along the hydrogen bonds and zero-point motion, respectively.

From our path integral simulations, we can estimate the spread of the proton wavefunction (see Fig. 4 legend for a precise definition)

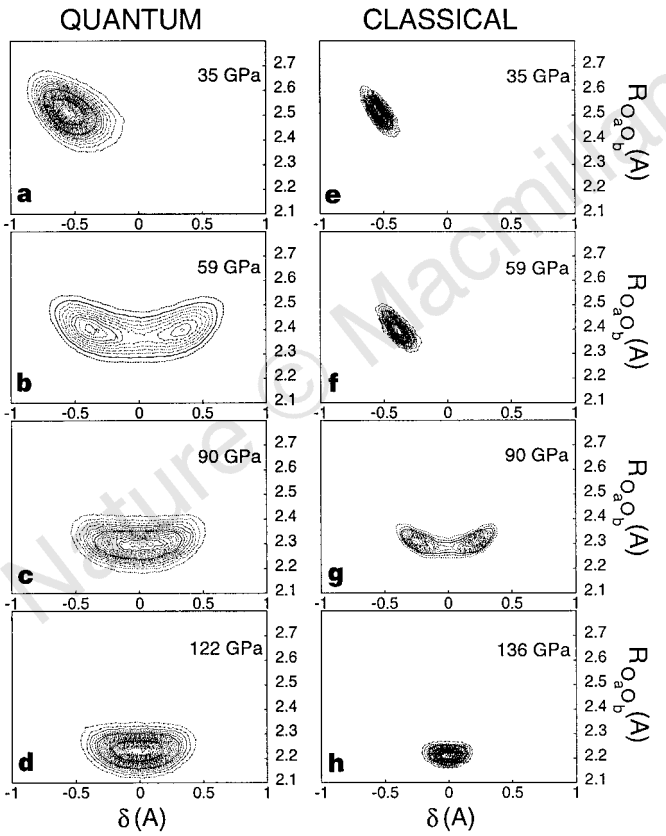

Figure 3 Proton symmetrization as a function of shortening of the hydrogen bond. Here we show contour plots of the average proton distribution function $P(\delta, R_{O_aO_b})$ as a function of the proton position relative to the bond midpoint $\delta = R_{O_aH} - R_{O_bH}$ and the corresponding oxygen–oxygen separation $R_{O_aO_b}$ for quantum (left panels) and classical (right panels) simulations at several representative volumes and 100 K; note that $\delta = 0$ corresponds to the proton being located midway between its neighbouring oxygen atoms O_a and O_b, irrespective of the actual $R_{O_aO_b}$ distance. Quantum: **a**, $V = 7.42\,cm^3\,mol^{-1}$ (~35 GPa); **b**, $V = 6.45\,cm^3\,mol^{-1}$ (~59 GPa); **c**, $V = 5.74\,cm^3\,mol^{-1}$ (~90 GPa); **d**, $V = 5.25\,cm^3\,mol^{-1}$ (~122 GPa); classical: **e**, $V = 7.42\,cm^3\,mol^{-1}$ (~35 GPa); **f**, $V = 6.45\,cm^3\,mol^{-1}$ (~59 GPa); **g**, $V = 5.74\,cm^3\,mol^{-1}$ (~90 GPa); **h**, $V = 5.08\,cm^3\,mol^{-1}$ (~136 GPa). For pressure conversion, see Fig. 1.

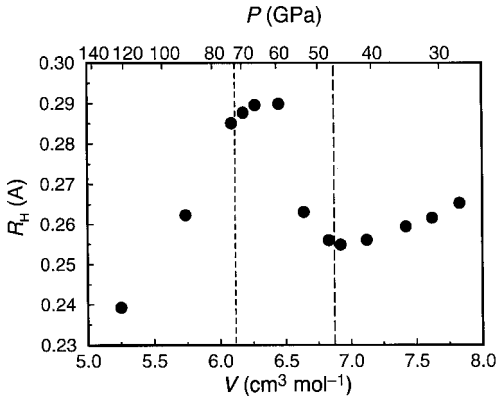

Figure 4 Evolution of the average spread of the quantum protons R_H as a function of the molar volume V at 100 K. We define the correlation function[29] $R_H(\Delta\tau) = \Sigma_{l=1}^{N} \left\langle |\mathbf{R}_l(\tau) - \mathbf{R}_l(\tau')|^2 \right\rangle^{1/2} / N$, where $0 \leqslant \Delta\tau = \tau - \tau' \leqslant \hbar\beta$, $\beta = 1/k_BT$, $\mathbf{R}_l(\tau)$ denotes the position of the lth proton at imaginary time τ; note that $R_H(\Delta\tau) \equiv 0$ Å for classical protons. The midpoint value $R_H = R_H(\hbar\beta/2)$ is a measure of the particles' spatial extents, whereas its variation in imaginary time (not shown here) determines the degree of ground-state dominance and thus localization[29]. Localized protons with a large energy gap ΔE between ground and excited states are characterized by a constant function in the range of roughly $\hbar/\Delta E < \Delta\tau < \hbar\beta - \hbar/\Delta E$, whereas $R_H(\Delta\tau)$ varies in the entire $\Delta\tau$ interval for extended or delocalized protons. The long-dash and short-dash vertical lines mark the VIII → VII and VII → X transitions, respectively, as a function of increasing pressure. For pressure conversion, see Fig. 1.

Nature © Macmillan Publishers Ltd 1998

Nature © Macmillan Publishers Ltd 1998

and get a glimpse of the structure of the proton excited states[29,30]. The results depicted in Fig. 4 as a function of pressure further strengthen our conclusions. Upon compressing ice VIII, we find that the protons become increasingly compact, ground-state dominated and thus localized. Overstepping the phase boundary to ice VII (long dashed line), their spatial extent increases rapidly and is accompanied by a strong delocalization: that is, extended protonic states contribute significantly in addition to the ground state. Such behaviour is also characteristic immediately after crossing the phase transition to ice X (short dashed line), but there is a clear trend for protons to become strongly localized again at the highest pressure, where the underlying potential is of the single-well type.

Our essential findings can be summarized as follows: (1) The sequence of the transitions is antiferroelectric ice VIII to paraelectric ice VII and finally to symmetric ice X at about 100 K; (2) the isotope effect on the antiferroelectric disordering transition (VIII → VII) is caused by translational proton tunnelling, whereas that on symmetrization (VII → X) is a qualitative zero-point motion effect; and (3) there are two 'forms' of ice X, both characterized by a unimodal proton distribution centred at the bond midpoint, the one at lower pressure being characterized by an underlying double-well proton transfer potential and a very broad proton distribution, whereas the high-pressure form has a single-well potential with a sharper proton localization. We hope that the insight we have gained from the different regimes of a 'clean' and relatively simple system, ice under controlled high pressure, will be useful in understanding quantum effects in other proton-transfer systems. □

Received 15 October 1997; accepted 7 January 1998.

1. Bernal, J. D. & Fowler, R. H. A theory of water and ionic solutions, with particular reference to hydrogen and hydroxyl ions. *J. Chem. Phys.* **1,** 515–548 (1933).
2. Pauling, L. The structure and entropy of ice and of other crystals with some randomness of atomic arrangement. *J. Am. Chem. Soc.* **57,** 2680–2684 (1935).
3. Bjerrum, N. Structure and properties of ice. *Science* **115,** 385–390 (1952).
4. Schweizer, K. S. & Stillinger, F. H. High pressure phase transitions and hydrogen-bond symmetry in ice polymorphs. *J. Chem. Phys.* **80,** 1230–1240 (1984).
5. McMahon, M. I. *et al.* Geometric effects of deuteration on hydrogen-ordering phase transitions. *Nature* **348,** 317–319 (1990).
6. Krumhansl, J. A. Sorting chickens from eggs. *Nature* **348,** 285–286 (1990).
7. Lee, C., Vanderbilt, D., Laasonen, K., Car, R. & Parrinello, M. *Ab initio* studies on high pressure phases of ice. *Phys. Rev. Lett.* **69,** 462–465 (1992).
8. Lee, C., Vanderbilt, D., Laasonen, K., Car, R. & Parrinello, M. *Ab initio* studies on the structural and dynamical properties of ice. *Phys. Rev. B* **47,** 4863–4872 (1993).
9. Holzapfel, W. B. On the symmetry of the hydrogen bonds in ice VII. *J. Chem. Phys.* **56,** 712–715 (1972).
10. Pruzan, P., Chervin, J. C. & Canny, B. Stability domain of the ice VIII proton-ordered phase at very high pressure and low temperature. *J. Chem. Phys.* **99,** 9842–9846 (1993).
11. Pruzan, P. Pressure effects on the hydrogen bond in ice up to 80 GPa. *J. Mol. Struct.* **322,** 279–286 (1994).
12. Goncharov, A. F., Struzhkin, V. V., Somayazulu, M. S., Hemley, R. J. & Mao, H. K. Compression of ice to 210 Gigapascals: Infrared evidence for a symmetric hydrogen-bonded phase. *Science* **273,** 218–220 (1996).
13. Aoki, K., Yamawaki, H., Sakashita, M. & Fujihisa, H. Infrared absorption study of the hydrogen-bond symmetrization in ice to 100 GPa. *Phys. Rev. B* **54,** 15673–15677 (1996).
14. Struzhkin, V. V., Goncharov, A. F., Hemley, R. J. & Mao, H.-k. Cascading Fermi resonances and the soft mode in dense ice. *Phys. Rev. Lett.* **78,** 4446–4449 (1997).
15. Marx, D. & Parrinello, M. *Ab initio* path-integral molecular dynamics. *Z. Phys. B (Rapid Note)* **95,** 143–144 (1994).
16. Marx, D. & Parrinello, M. *Ab initio* path integral molecular dynamics: Basic ideas. *J. Chem. Phys.* **104,** 4077–4082 (1996).
17. Tuckerman, M. E., Marx, D., Klein, M. L. & Parrinello, M. Efficient and general algorithms for path integral Car–Parrinello molecular dyanamics. *J. Chem. Phys.* **104,** 5579–5588 (1996).
18. Hobbs, P. V. *Ice Physics* (Clarendon Press, Oxford, 1974).
19. Nelmes, R. J. *et al.* Neutron diffraction study of the structure of deuterated ice VIII to 10 GPa. *Phys. Rev. Lett.* **71,** 1192–1195 (1993).
20. Aoki, K., Yamawaki, H. & Sakashita, M. Pressure-tuned Fermi Resonance in ice VII. *Science* **268,** 1322–1324 (1995).
21. Aoki, K., Yamawaki, H. & Sakashita, M. Observation of Fano interference in high-pressure ice VII. *Phys. Rev. Lett.* **76,** 784–786 (1996).
22. Hama, J. & Suito, K. Evidence of a new phase of ice above 70 GPa from the analysis of experimental data using the universal equation of state. *Phys. Lett. A* **187,** 346–350 (1994).
23. Pruzan, P. *et al.* Raman scattering and X-ray diffraction of ice in the Megabar range. Occurrence of a symmetric disordered solid above 62 GPa. *J. Phys. Chem. B* **101,** 6230–6233 (1997).
24. Wolanin, E. *et al.* Equation of state of ice VII up to 106 GPa. *Phys. Rev. B* **56,** 5781–5785 (1997).
25. Ceperley, D. M. Path integrals in the theory of condensed helium. *Rev. Mod. Phys.* **67,** 279–355 (1995).
26. Jones, R. O. & Gunnarsson, O. The density functional formalism, its applications and prospects. *Rev. Mod. Phys.* **61,** 689–746 (1989).
27. Hemley, R. J. *et al.* Static compression of H_2O-ice to 128 GPa (1.28 Mbar). *Nature* **330,** 737–740 (1987).
28. Nelmes, R. J., Loveday, J. S., Marshall, W. G., Besson, J. M., Klotz, S. & Hamel, G. Structures of ice VII and ice VIII to 20 GPa. *Proceedings of the International Conference on High Pressure Science and Technology (Joint Conference: AIRAPT-16 & HPCJ-38)* (Kyoto, August 25–29, 1997).
29. Chandler, D. & Leung, K. Excess electrons in liquids, geometrical perspectives. *Annu. Rev. Phys. Chem.* **45,** 557–591 (1994).
30. Štich, I., Marx, D., Parrinello, M. & Terakura, K. Proton-induced plasticity of hydrogen clusters. *Phys. Rev. Lett.* **78,** 3669–3672 (1997).
31. Becke, A. D. Density–functional exchange–energy approximation with correct asymptotic behavior. *Phys. Rev. A* **38,** 3098–3100 (1988).
32. Perdew, J. P. & Zunger, A. Self-interaction correction to density-functional approximations for many-electron systems. *Phys. Rev. B* **23,** 5048–5079 (1981).
33. Troullier, N. & Martins, J. L. Efficient pseudopotentials for plane-wave calculations. *Phys. Rev. B* **43,** 1993–2006 (1991).

Acknowledgements. Our warm thanks to M. Tuckerman, J. Hutter, U. Schwarz, M. Bernasconi and S. Klotz for useful discussions. The simulations were carried out on the IBM SP2 at CNUSC (Montpellier) and at MPI Stuttgart.

Correspondence should be addressed to D.M. (marx@prr.mpi-stuttgart.mpg.de).

Polarizing energy transfer in photoluminescent materials for display applications

Andrea Montali, Cees Bastiaansen, Paul Smith & Christoph Weder

Department of Materials, Institute of Polymers, ETH Zürich, CH-8092 Zürich, Switzerland

Combinations of sheet polarizers and colour filters form the basis of numerous products[1–4]—most notably colour liquid-crystal displays[2,4]—that require polarized chromatic light. But this combination of elements does not make efficient use of light, as a substantial fraction of the incident light is converted into thermal energy[3,4], limiting the brightness and energy efficiency of the resulting devices. Here we show that these limitations can be overcome by using polymer-based photoluminescent polarizers. Our polarizers operate on a two-step principle: randomly orientated 'sensitizer' molecules harvest the incident light by isotropic absorption and then efficiently transfer the energy to a uniaxially orientated photoluminescent polymer, from which coloured light with a high degree of linear polarization is emitted. In principle, isotropic-to-polarized conversion efficiencies approaching unity could be attainable by this approach.

The present limitations of liquid-crystal displays (LCDs) have recently triggered the development of polarizers based on selective reflection or scattering of light[5–9] which can replace the dichroic polarizer in a conventional LCD configuration. Using appropriate supplementary elements to recycle reflected or scattered energy, the ultimate efficiency of these systems can, in principle, approach unity (thus, twice that of dichroic polarizers); but in practice the efficiency is up to 80% (refs 5–9). However, colour applications require filters, which absorb at least two-thirds of the light[4], and thus reduce the ultimate overall efficiency to below 30%. In another recent approach, photoluminescent (PL) polarizers were shown to combine efficiently the polarization of light and the production of bright colours[10,11], together with a substantial increase in brightness and efficiency of PL LCDs based on these elements[12,13]. These polarizers comprise uniaxially orientated PL polymers, which, after photoexcitation, emit linearly polarized light. Their efficiency is chiefly limited by the luminophore's quantum yield which, ultimately, can approach unity, but for PL polymers is typically up to 80% (refs 14, 15). However, when used in a standard PL LCD configuration[12], only ~50% of light incident from the light source is used, as the absorption of these PL polarizers is also anisotropic[10,11].

We report here materials that show nearly isotropic absorption, but which emit the absorbed energy in highly polarized fashion, and, consequently, allow the production of PL polarizers that approach the ultimate efficiency. Such polarizers can directly replace the standard polarizer in conventional LCDs and, using an appropriate (ultraviolet) backlight and a dichroic mirror (to direct

Nature © Macmillan Publishers Ltd 1998

Nature © Macmillan Publishers Ltd 1998